Journal of Materials Chemistry A

Molecular Mechanisms of Thermal Instability in Hybrid Perovskite Light Absorbers for Photovoltaic Solar Cells

Journal:	*Journal of Materials Chemistry A*
Manuscript ID	TA-ART-05-2020-005356.R1
Article Type:	Paper
Date Submitted by the Author:	04-Aug-2020
Complete List of Authors:	Wang, Mingchao; Monash University, Department of Materials Science and Engineering Vasudevan, Vallabh; Monash University, Department of Materials Science and Engineering Lin, Shangchao; Shanghai Jiao Tong University, Institute of Engineering Thermophysics, School of Mechanical and Power Engineering Jasieniak, Jacek; Monash University, Materials Science and Engineering Russo, Salvy; RMIT University, Applied Physics Birbilis, Nick; Australian National University, College of Engineering and Computer Science Medhekar, Nikhil; Monash University, Department of Materials Science and Engineering

Molecular Mechanisms of Thermal Instability in Hybrid Perovskite Light Absorbers for Photovoltaic Solar Cells

Mingchao Wang[†*], Vallabh Vasudevan[†], Shangchao Lin[‡], Jacek Jasieniak[†], Salvy P. Russo[ǁ], Nick Birbilis[§] and Nikhil V. Medhekar[†*]

[†]Department of Materials Science and Engineering, Monash University, Faculty of Engineering, Wellington Road, Clayton, Victoria 3800, Australia

[‡]Institute of Engineering Thermophysics, School of Mechanical and Power Engineering, Shanghai Jiao Tong University, Shanghai 200240, China

[ǁ]ARC Centre of Excellence in Exciton Science, School of Science, RMIT University, Melbourne, Victoria 3001, Australia

[§]College of Engineering and Computer Science, Australian National University, Acton ACT 2601, Australia

*Corresponding Authors: mingchao.wang@monash.edu (Dr. Mingchao Wang); nikhil.medhekar@monash.edu (A/Prof. Nikhil V. Medhekar).

Abstract: The organic-inorganic hybrid perovskites have been widely explored as key functional components for energy harvesting/conversion applications due to their superior photovoltaic properties. However, material stability issues, such as temperature induced instability of hybrid perovskite crystals during normal device operating conditions, limit their practical application. Here we conduct molecular dynamics simulations to investigate the thermal instability in pristine as well as defective crystals of the prototypical organic-inorganic hybrid perovskite, methylammonium lead iodide ($MAPbI_3$). We show that the accumulation of tilting and splitting of PbI_6 octahedra with increasing temperatures initiates the instability in pristine $MAPbI_3$ crystals. Point defects can accelerate the inception of local lattice instability, and the crystals with such defects in the concentration range typically observed in perovskite-based devices undergo an irreversible instability at much lower temperatures. Two-dimensional defects such as grain boundaries in polycrystalline $MAPbI_3$ crystals further decrease their crystal instability temperature to about 550 K, in a good agreement with experimental measurements. Finally, we demonstrate that thermal instability in $MAPbI_3$ thin films originates from their free surfaces at much lower temperatures due their increased free energies. We also investigate the structural evolution of the local lattice and show that Born and Lindemann crystal instability criteria coincide in initiating the instability. The key insights obtained from this work can usher a rational design of highly stable hybrid perovskites for their robust and reliable photovoltaic applications.

1. Introduction

Hybrid organic-inorganic perovskites have rapidly emerged as promising light absorbers in the next-generation of highly efficient solar cells owing to their superior power conversion efficiency.[1, 2] For example, the demonstrated power conversion efficiency of single junction hybrid perovskite solar cells has increased from ~12% to ~22.0% in just last five years.[3, 4] Incorporating perovskites as light absorbers on top of silicon solar cells in a two- and four-terminal tandem configurations has further raised the efficiency up to 26% and ~23.6%, respectively.[5, 6] However, recent studies have shown that various processing and operating conditions (for example, type of device architecture, deposition/evaporation routes during processing, operating temperature, moisture and UV exposure) are likely to trigger thermal, mechanical and chemical instabilities in active hybrid perovskite absorber crystals, resulting in the performance degradation and failure of solar cell devices.[7, 8] These material stability issues pose a serious challenge to the commercialization of perovskite-based solar cells, since at present they cannot maintain an uninterrupted 25 years-long operation that is essential for their commercial feasibility.[9]

Among various material instabilities in hybrid perovskites, the instability caused by exposure to higher temperatures plays a key role in their practical operation, since any type of thin-film photovoltaic modules are expected to experience temperatures as high as 85 °C during their standard operation.[10] Recently, experimental studies have reported on the thermal decomposition, followed by the sublimation of the prototype hybrid perovskite methylammonium lead iodide ($MAPbI_3$), and showed that it generally decomposes into ionic and organic components.[11] However, these studies provide little clarity on the thermal decomposition temperature,[11, 12] as well as the sublimation reactions, largely due to the widely varying experimental conditions.[13-15] In

general, the first step of the $MAPbI_3$ decomposition is likely the onset of an instability in the crystal, followed by the chemical decomposition of organic cations. For example, thermogravimetric measurements demonstrated that the crystal decomposition of $MAPbI_3$ powders starts within the temperature range of 520 K to 690 K, subsequently followed by the formation of gaseous byproducts.[11, 14, 16-21] In contrast, conductive atomic force microscopy analyses showed that polycrystalline $MAPbI_3$ decomposes at a lower temperature (~360 K) in the nitrogen environment after 24 hours.[22] Even though environmental factors may play a role in the thermal stability of hybrid perovskites, these contradicting results can be attributed to the yet unclear molecular-level mechanisms in the thermally-induced instability of the $MAPbI_3$ crystal. As for the thermal behavior of non-prototypical hybrid perovskites, very recent reports have suggested that low-dimensional structures[23] and the substitution of MA with formamidinium[24] or caesium[25] can efficiently improve the thermal stability of mixed-halide perovskites. Therefore, a clearer understanding of the underlying mechanisms of the thermal instability of $MAPbI_3$ can be expected to enable an optimal design and synthesis of stable hybrid perovskites.

For the practical applications of hybrid perovskites, their thermal stability is greatly influenced by the presence of intrinsic defects in their crystal structures. Solution-processed hybrid perovskites inevitably contain point defects (i.e. vacancies)[26, 27] and structural disorders, such as free surfaces and twin or grain boundaries in polycrystalline thin films.[28, 29] Experiments have indicated that these structural defects degrade the stability and performance of the functional devices, to the level much below that of defect-free hybrid perovskites.[30-32] For instance, it has been suggested that the disorder-weakened Pb-I bonding network at grain boundaries can accelerate the crystal and chemical decomposition of polycrystalline $MAPbI_3$.[32] Electric field and light can further enhance

ion migration in $MAPbI_3$, due to the intrinsic structural defects, especially of I^- ions with a low migration energy barrier (~0.1 eV).[33-35] Such enhanced ion migration is believed to result in the observed current-voltage hysteresis phenomena[36, 37] and switchable photovoltaic effects[38] in the $MAPbI_3$-based photovoltaic solar cells. Although recent studies have confirmed the resilience of electronic properties of $MAPbI_3$ to point defects,[39, 40] a quantitative understanding of the relationship between structural defects and crystal stability in hybrid perovskites is not yet available.

In addition to experimental measurements, recent computational studies have also reported the degradation of hybrid perovskites. For example, first-principles calculations have shown that the formation of partial Schottky defect (charge neutral MAI^0 vacancy) is energetically favorable in $MAPbI_3$, and possibly leads to the decomposition of $MAPbI_3$.[39] Under humid conditions, the $[PbI_2]^0$-terminated surface is more stable than the $[MAI]^0$-terminated surface, which undergoes a rapid dissolution process[41] and forms hydrated compound $MAPbI_3 \cdot H_2O$.[42] However, the underlying atomic-scale mechanisms of the dynamic process of the crystal degradation in hybrid perovskites have been rarely investigated by first-principles calculations, due to the intrinsic length- and time-scale limitations. Alternatively, large-scale classical molecular dynamics (MD) simulations have been successfully conducted to explore fundamental properties of $MAPbI_3$,[43-45] as well as its water-induced degradation,[46, 47] showing good agreement with experimental results.

To understand the underlying mechanisms of thermal instability in hybrid perovskite light absorbers, here we perform classical molecular dynamics (MD) simulations to investigate the thermal-induced crystal instability of the prototype hybrid perovskite $MAPbI_3$. We examine the

role played by a range of intrinsic crystalline defects, including point vacancies, free surfaces and twin or grain boundaries, in controlling the stability of $MAPbI_3$ crystals. We first construct the relationship between the onset of the instability and the corresponding microstructural evolution in the defect-free $MAPbI_3$ crystal induced by elevated temperatures. Our atomistic simulations demonstrate that a gradually increasing tilt in the PbI_6 octahedra and breaking of the octahedral network initiates a local instability in the crystal structure, which progressively spreads further in the pristine $MAPbI_3$ crystal. Point defects can accelerate the accumulation and coalescence of these local lattice instabilities, and as a result facilitate an irreversible instability at lower temperatures. In addition, twin and grain boundaries trigger the instability of $MAPbI_3$ crystals at much lower temperature than the point defects, in some cases, lower than by as much as 200 K compared to defect free crystals. We further apply Born and Lindemann criteria to develop a fundamental understanding of the thermal instability in $MAPbI_3$ crystals. Finally, our kinetic and thermodynamic investigation confirms that the crystal instability in thin films initiates from their free surfaces, again at a much lower temperature compared to the bulk crystal. These fundamental insights into the thermal instability in $MAPbI_3$ and the role played by various intrinsic defects, can inspire optimal design of robust and high-performance hybrid perovskite photovoltaics.

2. Computational Methods

2.1 Simulation of thermal instability

To fully capture the slow dynamics of crystal decomposition of $MAPbI_3$, atomic-level molecular dynamics simulations at significantly large time and length scales are required to allow a predictive modeling of thermal stability, which are typically out of reach for the most first principles based methods. Therefore, here we perform classical molecular dynamics (MD) simulations

incorporating temperature-induced anharmonic effects. All our MD simulations are carried out using the open-source code LAMMPS[48] and classical potential MYP1, which is calibrated to accurately describe the interatomic interactions in the complex organometallic structure of $MAPbI_3$.[43, 46] In the MYP1 potential, the pairwise interactions between (Pb, I)-(Pb, I) and (Pb, I)-(C, N) pairs are modeled by Buckingham and Coulombic potentials, while Lennard-Jones (LJ) and Coulombic potentials are employed to define the intra-/inter-molecular interactions of MA molecules.[46] The detailed potential parameters for all intra-/inter-molecular interactions used in our MD simulations are given in **Table S1** in **Electronic Supplementary Information** (**ESI**). Although these potentials do not explicitly include the bond angle interactions, when compared to experiments and first-principles calculations, they reproduce fundamental structural, dynamical and physical properties of $MAPbI_3$, such as its phase diagram,[43, 46] thermal transport,[44] crystallization,[49] point-defect diffusivity,[35] as well as elastic and fracture behavior.[45] The particle-particle particle-mesh (PPPM) method[50] is adopted here to treat long-range Coulombic interaction via the reciprocal space, since this method is significantly faster than the regular Ewald summation method.[51] The cutoff distance of 1 nm is used for all short-range (Buckingham and LJ) and long-range (Coulombic) interactions. A time step of 0.5 fs is selected for all MD simulations.

To investigate the thermal stability behavior of $MAPbI_3$, various material models of the bulk crystal structure, with defects such as vacancies and grain boundaries, as well as of thin films with free surfaces, are considered in this work. Recent first principles calculations have shown that charge neutral (100) surfaces of cubic $MAPbI_3$ are energetically stable compared to surfaces with other crystalline orientations, and their electronic structures also contribute to the long carrier lifetimes in solar cell devices.[52, 53] Thus we consider two stable, charge neutral (100)/$[MAI]^0$- and

(100)/$[PbI_2]^0$-terminated surfaces in our thin film models. As mentioned earlier, since structural defects, and in particular, point defects such as vacancies are inevitably introduced in $MAPbI_3$ during synthesis process, we also study the influence of ionic MA^+ (V_{MA}) and I^- (V_I) point vacancies and the charge neutral MAI^0 (V_{MAI}) vacancy on the thermal stability of $MAPbI_3$. In order to compare the results obtained from the model to experimental conditions, we have also considered bicrystal models as well as polycrystalline models with randomly oriented grain boundaries. In order to identify the mechanisms of thermal instability in $MAPbI_3$, we simulate the thermal-induced crystal instability of both $MAPbI_3$ bulk crystals and thin films at elevated temperatures and analyze their corresponding microstructural evolution at the molecular level. All simulation models are first equilibrated at room temperature for 1 ns, and then gradually heated to a higher temperature (much below instability temperature T_c) at a heating rate of 0.5 K/ps. To ensure that models are fully equilibrated, they are heated further with an incremental temperature of 2.5 K up to T_c, and equilibrated for 50 ps at every incremental step (an approximate heating rate of 0.05 K/ps) under *NPT* ensemble with an isotropic pressure of 1 bar using the Nosé-Hoover thermostat and barostat.[54, 55] It should be noted that the heating rate in simulations is significantly higher than that in the experiments. Such unrealistically rapid heating can lead to the artificial out-of-equilibrium states of the $MAPbI_3$ crystal, resulting in the accelerated material degradation at much lower value of T_c. Following previous work,[56] the selected heating rate of 0.05 K/ps here minimizes out-of-equilibrium distortions of the crystal for a reasonable prediction of T_c for $MAPbI_3$. The atomic configurations from all models are then used to explore the microstructural evolution during the thermal instability process.

2.2 Calculation of elastic properties

In order to understand the mechanisms of structural instability in hybrid perovskites, we evaluate the elastic properties of $MAPbI_3$ bulk crystals to explore their lattice instability based on the Born criterion.[57, 58] We employ the direct method based on constant volume MD simulations to predict the elastic constants of cubic $MAPbI_3$ crystals at 0 K as well as at elevated temperatures. Under a small strain $\varepsilon_{xx} = e$, we have the following relations for the cubic crystal symmetry:

$$\sigma_{xx} = C_{11}e \quad , \quad \sigma_{yy} + \sigma_{zz} = 2C_{12}e \tag{1}$$

Atomic normal stresses σ_{xx}, σ_{yy} and σ_{zz} are obtained from the ensemble averages, and elastic constants C_{11} and C_{12} can be calculated from Eq. (1). C_{44} can be obtained from the relation $\tau_{xy} = C_{44}e$. For cubic $MAPbI_3$, the elastic constants C_{11} and C_{12} and C_{44} are averaged along all three directions. In our *NVT* simulations, we have explicitly calculated both the stress-fluctuation and thermal contributions to the temperature dependent elastic properties using the expression[59, 60]

$$C_{ijkl}^{stress-thermal} = -\frac{V}{k_B T}\left(\left\langle \sigma_{ij}\sigma_{kl} \right\rangle - \left\langle \sigma_{ij} \right\rangle \left\langle \sigma_{kl} \right\rangle\right) + C_{ijkl}^{K} \tag{2}$$

where σ is atomic stress, V is the total volume of the simulation model, k_B is the Boltzmann constant, T is the temperature, the tensor indices i, j, k, l can be simplified by Voigt's notation. The first term is the contribution from the stress fluctuation, and the second term C_{ijkl} is the kinetic (thermal) contribution, which can be expressed as:

$$C_{ijkl}^{K} = \frac{2Nk_B T}{V}\left(\delta_{ik}\delta_{jl} + \delta_{il}\delta_{jk}\right). \tag{3}$$

Here we have calculated the stress-fluctuation term by time averaging and the thermal term by the analytical expression Eq. (3).

2.3 Calculation of amplitude of atomic vibrations and phonon dispersion

To understand the thermal-induced crystal instability of $MAPbI_3$ by thermodynamic Lindemann criterion, we estimate the amplitudes of atomic vibrations of different ionic species. Simulation models are first fully relaxed till they reach their equilibrium states under *NPT* ensemble. The mean square displacements (MSDs) of ionic species on short time scales are calculated according to the equation:

$$\mathrm{MSD}=\left\langle \Delta r^2 \right\rangle = \left\langle \sum_{i=1}^{3} \left| r_i(t) - r_i(0) \right|^2 \right\rangle = \frac{1}{N} \sum_{j=1}^{N} \sum_{i=1}^{3} \left| r_i^j(t) - r_i^j(0) \right|^2 \tag{4}$$

where N is the total atom number; $\langle \cdots \rangle$ denotes the average value over all atoms; $r_i(0)$ and $r_i(t)$ are i-axis positions at time 0 and t. The calculated MSDs is nearly constant with respect to time and contains only the vibrational but not the diffusional contribution. Then, the amplitude of atomic vibration is obtained as the root mean square displacements. To obtain phonon dispersion curves at finite temperatures, we calculated the dynamical matrix from MD simulations based on fluctuation-dissipation theorem, see **Section S2** in **ESI** for more details.[61]

3. Results and Discussion

3.1 Thermal instability of $MAPbI_3$ bulk crystal

We first investigate the thermal instability of pristine, defect-free $MAPbI_3$ bulk crystal. As seen in **Figure 1b** and animation **V1**, with increasing temperature, the atomic structure of $MAPbI_3$ undergoes a sharp transition from the crystalline to a disordered state at a critical temperature T_c, followed by the loss of MA ions as reported in several experiments.[11, 12] T_c therefore characterizes the initiation of a thermal instability of the crystal or the phase transition from the crystalline structure. In such first-order transitions, the mean atomic volume undergoes a sharp increase at the critical temperature T_c.[62] Consequently, tracking changes in the mean atomic volume Ω (defined

as the total volume divided by the number of MA^+, Pb^{2+}, and I^- species) as a function of temperature enables the determination of T_c as shown in **Figure 1b**. It is clear that $MAPbI_3$ crystal becomes unstable at ~1050 K with a critical value of Ω_{cr} ~57.7 Å^3. To understand the evolution of the crystal structure during the onset of thermal instability, we also evaluate temperature dependent translational order parameter η as,

$$\eta = \left\langle \left| \frac{1}{3N} \sum_{n=1}^{N} \sum_{q}^{3} \exp(i\mathbf{k}_q \cdot \mathbf{r}_n) \right|^2 \right\rangle = \left\langle \left| \frac{1}{3N} \sum_{n=1}^{N} \sum_{q}^{3} \cos(\mathbf{k}_q \cdot \mathbf{r}_n) \right|^2 + \left| \frac{1}{3N} \sum_{n=1}^{N} \sum_{q}^{3} \sin(\mathbf{k}_q \cdot \mathbf{r}_n) \right|^2 \right\rangle \quad (5)$$

where $\mathbf{k}_q$ is the reciprocal lattice vector, $\mathbf{r}_n$ is the position vector of atom n, N is the total number of atoms in the simulation model. η equals 1 in the ideal crystal state at 0 K, while it fluctuates near zero in the fully disordered state. As seen in **Figure 1b**, a sudden drop of η from 0.32 to 0 at T_c ~1050 K represents a crystalline to disordered phase transition. **Figure 1c** shows the variation of several microstructural parameters such as the tilting angle and the coordination numbers with temperature. It is evident that increasing temperature results in a progressively increasing tilting of the PbI_6 octahedra, which is revealed by a steady reduction in the average Pb-I-Pb octahedral tilting angle θ at the rate of 0.0158°/K. Such tilting deformation of octahedra is relatively homogeneous with a small average fluctuation $\Delta\theta_{ave}$ of 1.8°.

The analysis of the radial distribution functions (see **S1** and **Figure S1** in **ESI**) and the coordination numbers (N) demonstrates that although PbI_6 octahedra are highly stretched and distorted (average bond lengths of Pb-I and I-I pairs at temperatures above 800 K are much larger than at 300 K), the octahedral network is largely intact with a very small fraction of partial octahedra (i.e. PbI_4 and PbI_5) and a corresponding small decrease in the average coordination of Pb and I ions. This high degree of crystalline integrity is maintained until the temperature reaches a critical value T_c ~1050

K, after which a large number of structural defects quickly turn the crystal into its disordered phase, with $N_{Pb} \approx 5.84$ and $N_I \approx 1.87$ (**Figure 1d**). It should be noted that such microstructural evolution of $MAPbI_3$ during crystal decomposition is characteristically different than in other classes of materials such as metals[63, 64] and colloidal crystals.[65] For instance, several studies have shown that the formation and migration of point/localized defects or dislocations driven by thermal fluctuation initiates the crystal instability of pristine crystals of Cu and Al, unlike the tilting and breaking of octahedral network that dominates the crystal instability of the pristine $MAPbI_3$ crystal.[63, 64]

3.2 Effect of point defects on the thermal instability of $MAPbI_3$ crystals

Since $MAPbI_3$ is experimentally found to have large defect concentrations—for example, the concentration of partial Schottky MAI^0 vacancy can be as large as 3.82%[39]—we now explore the influence of three types of vacancies, namely, I^- (V_I), MA^+ (V_{MA}), and MAI^0 (V_{MAI}), on the thermal instability of the $MAPbI_3$ crystal (see animations **V2** for V_I, **V3** for V_{MA}, and **V4** for V_{MAI}). **Figure 2a** shows that the increasing concentration of point vacancies leads to a remarkable reduction in T_c of $MAPbI_3$. In particular, V_{MAI} defect results in a lower T_c than V_I and V_{MA} at the same level of vacancy concentration, indicating a strong mixed-vacancy effect on the thermal stability of the crystal. As shown in **Figure 2b**, the critical values of atomic mean volume of defective $MAPbI_3$ (Ω_{cr}) are largely independent of both the defect concentration and the ionic species, and are close to that of a perfect crystal Ω_{cr} of ~57.7 $Å^3$. Such near equal magnitudes of Ω_{cr} for defect-free and defective $MAPbI_3$ crystals indicate that Ω_{cr} is an intrinsic indicator of the thermally induced crystal instability in $MAPbI_3$. As shown in **Figure S2** in **ESI**, for temperatures below T_c, due to additional free volume, point vacancies lead to increase in the Ω of defective $MAPbI_3$ compared to that of the perfect crystal at the same temperature, consequently leading to a lower temperature for the

onset of crystal instability of $MAPbI_3$ with increasing vacancy concentration. This feature describing the crystal instability in hybrid perovskite crystals is consistent with several classes of materials (for example, FCC metals), where the critical atomic volume is independent of the path by which its material phase is achieved, whether by heating the perfect crystal or via introducing point defects.[46]

Next we study the microstructural evolution of $MAPbI_3$ crystals with point defects during their thermal-induced crystal instability. **Figure 2c-d** exhibit the variation of critical microstructural parameters such as the tilting angles and the coordination numbers. **Figure 2c** shows that V_{MAI} induces a much lower critical value of θ_{ave} (θ_{ave}^{cr}) than V_I and V_{MA} defects at the same concentrations, revealing a significant tilting of PbI_6 octahedra before the onset of the instability. However, the analysis of critical coordination numbers shown in **Figure 2d** demonstrates that V_{MAI} maintains a better octahedral network than V_I as reflected by the much smaller value of $N_{\mathrm{Pb}}^{\mathrm{cr}}$. A seemingly contrasting trend between θ_{ave}^{cr} and $N_{\mathrm{Pb}}^{\mathrm{cr}}$ highlights that the tilting of PbI_6 octahedra rather than the integrity of the octahedral network itself dominates the thermal stability behavior of $MAPbI_3$ crystals. To establish this intrinsic relationship further, we also evaluate the temperature-dependent phonon properties of $MAPbI_3$ crystals for temperatures up to T_c (see **S2 Section** in **ESI** for details). Lattice dynamics simulations at 0 K reported in the literature have predicted negative frequency phonon modes at both R and M points in the Brillouin zone,[44] associated with certain metastable low symmetry structures that can be reached by the tilting of PbI_6 octahedra.[66] As shown in **Figure 3**, however, thermal fluctuations at temperatures above 300 K generate a more uniform distribution of MA ion orientation and suppress those local lower-symmetry structures, thus exhibiting positive frequencies at R and M point. With increasing

temperature, we can see the reduced frequencies of some phonon modes in both pristine and defective $MAPbI_3$ crystals. These softened phonon modes indicate large vibration amplitudes of the crystal structure, which can be attributed to certain local crystal deformation, such as tilting, distortion or splitting of PbI_6 octahedra.

We next briefly discuss a unique feature of the phonon properties in $MAPbI_3$ crystals with point defects. In the case of V_I defects the obvious fluctuations in phonon dispersion curves (**Figure 3b**) are associated with the diffusive I^- ions, which possess a remarkable ionic diffusivity compared with the almost negligible diffusion of Pb^{2+} and MA^+ ionic species.[35] The much lower frequencies of optical phonon modes at the Γ point, which are related to the larger crystal vibration amplitudes, also indicate the stronger diffusion of I^- ions in the crystal.[67] Moreover, phonon frequencies at both R and M points approach to zero with increasing temperature. This points to a severe tilting of PbI_6 octahedra, in good agreement with our previous analysis of the tilting angles in V_I-defective $MAPbI_3$. In the case of V_{MA} defect, phonon frequencies at the Γ point are much larger, and there is a small decrease in the frequencies at R and M points. This trend in the shapes of phonon dispersion curves is associated with a constrained diffusion of all ionic species and the tilt of PbI_6 octahedrons. As for the mixture of V_I and V_{MA}, they concurrently contribute to the greater ion diffusion and the severe tilting of PbI_6 octahedra, leading to the lattice instability of $MAPbI_3$ crystal at a much lower crystal instability temperature T_c.

3.3 Thermal instability of $MAPBI_3$ thin films—the effect of free surfaces

Since $MAPbI_3$ absorber layers in perovskite-based solar cells are normally synthesized by the inexpensive solution-based fabrication methods, two-dimensional defects such as free surfaces,

grain boundaries and twin boundaries grain boundaries inevitably exist in the as-fabricated $MAPbI_3$ thin films and can impact the structural stability. We first investigate the influence of stable, low energy, charge-neutral $[MAI]^0$ and $[PbI_2]^0$ free surfaces on the thermal stability of $MAPbI_3$ (see animations **V5** for $[MAI]^0$ and **V6** for $[PbI_2]^0$ in **ESI**). **Figure 4a** shows the variation of the mean atomic volume Ω for models with $[MAI]^0$ and $[PbI_2]^0$ free surfaces with increasing temperature. It can be seen that the thermal instability of the hybrid perovskite surfaces is characterized by a sudden change in the trend of the mean atomic volume at the crystal instability temperature (T_c) of ~ 600 K and ~ 635 K for $[PbI_2]^0$ and $[MAI]^0$ surfaces, respectively, representing the onset of the transition from the crystalline to an amorphous liquid phase. However, in contrast to the instability in bulk $MAPbI_3$ crystals, this transition is much more gradual due to a layer-by-layer crystal decomposition. The snapshots of atomic configurations in **Figure 4b** show the microstructural evolution of both free surfaces during such partial decomposition process.

To further understand this layer-by-layer crystal decomposition, we define the in-plane layer order parameter η_{layer} as,

$$\eta_{layer} = \left\langle \left| \frac{1}{2N} \sum_{n=1}^{N} \sum_{q}^{2} \exp(i\mathbf{k}_q \cdot \mathbf{r}_n) \right|^2 \right\rangle = \left\langle \left| \frac{1}{2N} \sum_{n=1}^{N} \sum_{q}^{2} \cos(\mathbf{k}_q \cdot \mathbf{r}_n) \right|^2 + \left| \frac{1}{2N} \sum_{n=1}^{N} \sum_{q}^{2} \sin(\mathbf{k}_q \cdot \mathbf{r}_n) \right|^2 \right\rangle \quad (5)$$

where $\mathbf{k}_q$ is the in-plane reciprocal lattice vector in each layer, $\mathbf{r}_n$ is the position vector of atom n, N is the total number of ions in the $[PbI_2]^0$ layer, as well as MA^+ and ionic components ($[MA]^{n+}$ and $[I]^{n-}$ partial layers) in the $[MAI]^0$ layer. As in the case of the bulk crystal, the extremum η_{layer} values of 0 and 1 represent the amorphous and crystalline states of each layer at 0 K. As shown in **Figure 4c** for the $[MAI]^0$-terminated surface, at the temperatures below the onset of instability (temperature less than 635K), the surface $[MA]^{n+}$ partial layer are generally less ordered (smaller

values of the parameter η_{layer}) than the surface $[I]^{n-}$ partial layer and other subsurface layers in the bulk. Furthermore, the zigzag fluctuation of η_{layer} for ionic components ($[PbI_2]^0$ layers and $[I]^{n-}$ partial layers) in the subsurface layers indicates that the $[MAI]^0$ subsurface layers are more disordered than the $[PbI_2]^0$ subsurface layers. As the temperature exceeds the instability temperature of 635K, the $[MAI]^0$ surface and the several subsurface layers become progressively disordered as a precursor to the instability of the crystal. The $[PbI_2]^0$-terminated surface (see **Figure 4d**) exhibits a similar behavior to that of $[MAI]^0$-terminated surface, except the crystal decomposition of the $[PbI_2]^0$ surface initiates at a lower temperature of 600 K.

From a thermodynamic point of view, a $MAPbI_3$ thin film with free surfaces is energetically less stable than the $MAPbI_3$ bulk crystal, and thus has much higher total free energy.[68, 69] Moreover, since such thin films with free surfaces report a small decrease of layer order parameters η_{layer} before the initiation of the thermal instability, we assume that the variation of entropy contribution to the total free energy with temperature is negligible. According to **Figure S3**, the free energy increase due to surfaces leads to the reduction of crystal instability temperature T_c of thin films with both $[PbI_2]^0$ and $[MAI]^0$ surfaces.[68] This can also apply to the size effect on the T_c of micro and nanoparticles, meaning that smaller particles have higher free energy per volume and thus a lower T_c.[70, 71] When temperature is at or above T_c, an amorphous layer starts to nucleate at the free surfaces since the amorphous phase is more energetically stable than the crystalline phase (see **Figure S3a** in **ESI**). In a solid-amorphous coexisting film, its free energy changes from G_{film} to $G_{film}' = G_{film} + \Delta G_{interface}$, where $\Delta G_{interface} = 2\gamma_{eff}/r$, and γ_{eff} is the effective interfacial free energy, r being the effective radius of the crystalline–amorphous interface.[72, 73] The decomposed $MAPbI_3$ thin film has $r = \infty$ and $G_{film}' = G_{film}$. The invariance of free energy of the coexistence determines

that the amorphous layer grows continuously until it consumes the entire model. Such continuous crystal decomposition process in thin films is different from that in the bulk crystals with nanovoids. According to the equation $G_{bulk\text{-}void}' = G_{bulk\text{-}void} + \Delta G_{interface}$, the bulk crystal with nanovoids (negative curvature) have lower free energy $G_{bulk\text{-}void}'$ compared to that of perfect bulk crystal $G_{bulk\text{-}void}$.[73] Consequently, the amorphous or liquid layer in the nanovoids stays stable in the absence of enough driving force to grow continuously (see **Figure S3b** in **ESI**). It should be noted that after the breaking of the octahedral network, organic components will quickly sublimate and the rest part will form PbI_2 clusters, which is consistent with a two-step decomposition reaction process observed in experiments.[11, 12] However, an investigation into sublimation reactions and the formation of PbI_2 clusters is beyond the scope of this study, which can be further explored using quantum mechanical simulations.

Among two $MAPbI_3$ surfaces considered here, the $[PbI_2]^0$ surface is less energetically stable than the $[MAI]^0$ surface, due to its higher surface enthalpy as suggested by earlier estimates in the literature (by ~0.45 eV/surface unit cell).[68] Consequently the instability of the crystal structure at the surface can be expected to set in at a lower temperature. The stability of $[MAI]^0$ surface is associated with its surface reconstruction,[74, 75] where the rearranged orientation of surface MA^+ cations strengthens their interactions with surface I^- anions and weakens the surface polarity.[74] In terms of the reduced T_c by vacancies and free surfaces, defective hybrid perovskite absorber layers in practical solar cells can have much lower thermal instability temperature, which should be further experimentally validated in future studies. Our predictions of the layer by layer degradation from $MAPbI_3$ surfaces are in good agreement with recent first-principles calculations, which indicates that such surface-initiated layer-by-layer decomposition represents the lowest energy

pathway for material decomposition.[76] However, an accurate estimation of byproducts after the crystal decomposition of $MAPbI_3$ crystals (for example, $NH_3(g) + CH_3I(g)$)[13-15]) is out of reach of the empirical potential utilized in this work.

3.4 Mechanisms of thermal instability in $MAPbI_3$ bulk crystals and thin films

To gain a deeper understanding of the temperature-induced instability, we explore the mechanisms for thermal instability in the simplest cases of bulk crystals and thin films of $MAPbI_3$. In general, two mechanisms, as described by Born and Lindemann criteria, have been proposed to understand the phase instability of crystals. Born criterion stipulates a *mechanical instability* resulting from the lattice instability[57, 58] and a spontaneous generation of structural defects inside the bulk solids.[56, 64] Such rigidity catastrophe arises at T_c when one of the two elastic shear moduli C_{44} and $C' = \left(C_{11} - C_{12}\right)/2$ vanishes, C_{11}, C_{12} and C_{44} being the elements of elastic constant matrix for the cubic crystal.[57] We therefore calculate both atomic volume (Ω) and temperature (T) dependent elastic constants and shear moduli of bulk $MAPbI_3$. Here the strain (Ω) loading at 0 K is equivalent to thermal (T) loading due to the temperature induced volume expansion.

Figure 5a illustrates that the shear modulus C' is much smaller than C_{44} for all values of Ω in the pristine $MAPbI_3$ crystal. Both C_{44} and C' shear moduli decrease with increasing Ω, and C' decreases to nearly zero as the temperature approaches to T_c due to the melting-induced lattice instability. Interestingly, a small rise of C' above T_c results from the liquid phase of bulk $MAPbI_3$. **Figures 5b-d** show the effect of point vacancies on C' of defective $MAPbI_3$. We can see in some cases (for example, for I^- vacancies at the concentration of 0.024 in **Figure 5b**) the shear modulus C' shows a non-uniform downward trend with respect to Ω. It is interesting to note that the calculated values

of C' do not show strong correlation with the type and even the concentration of point vacancies in the range of concentrations considered in this work. Such an observation can be attributed to the local lattice reconstruction caused by point defects may not soften the overall lattice stiffness. Similar to the pristine $MAPbI_3$ crystal, C' for $MAPbI_3$ crystals with point defects are also close to zero as Ω approaches its critical value. C' is also much smaller than C_{44} for all temperatures. **Figure 6** shows similar trend that the shear modulus C' decreases with temperature, and reduces to almost zero when temperature approaches T_c, owing to the accumulation of local lattice instabilities within $MAPbI_3$ crystals. The temperature ranges in **Figure 6** correspond to much larger values of Ω (> 56 Å^3) in **Figure 5**, and thus present smaller values of C' in **Figure 5**. It can be noted that the contributions of stress fluctuations and temperature to the shear moduli can be neglected, since these can be estimated to be ~0.1 GPa (see **Computational Methods**), which is about one order of magnitude smaller than the shear moduli.

The second criterion of the crystal instability, the Lindemann criterion, stipulates a *thermodynamic instability* of inhomogeneous solids, which initiates at structural defects such as vacancies and free surfaces.[56, 77-79] Crystal instability is initiated by a vibrational instability when the so-called Lindemann ratio (δ) between the amplitude of atomic vibration (equaling to root mean square displacement RMSD) and average nearest-neighbor distance reaches to a critical value δ_{cr}. Such value depends on the nature of interatomic interactions, magnitude of quantum effects and crystal structures.[80, 81] In $MAPbI_3$ thin films, **Figure 7** shows that $[PbI_2]^0$ and $[MAI]^0$ surfaces have larger amplitudes of atomic vibrations than interior subsurface layers before crystal instability. The instability of thin films starts when ions at free surfaces reach their irreversible atomic vibrations, and the critical values of δ, in good agreement with the analysis of the layer order η_{layer} presented

earlier that shows the crystalline to amorphous phase transition starts from free surfaces. Such thermodynamic analysis of surface decomposition is also consistent with earlier discussion on free energy as to why the crystal decomposition of $MAPbI_3$ thin films starts from their free surfaces.

We next discuss the relationship between the Lindemann criterion and microstructural evolution during the crystal instability of $MAPbI_3$ bulk crystals. It has been demonstrated that both Born and Lindemann criteria coincide for monoatomic bulk solids, where the crystal decomposition is initiated by local lattice instabilities.[56, 82] If an atom has its Lindemann ratio larger than δ_{cr}, it is defined as a Lindemann particle and generates local lattice instability. The accumulation and coalescence of these Lindemann particles govern the homogeneous instability nucleation inside the crystal.[56] Such kinetic mechanism can also be applied to the pristine $MAPbI_3$ crystal, and correlates with its microstructural evolution during the crystal decomposition. As discussed earlier, thermal energy can activate a strong tilting of PbI_6 octahedra. Owing to the central position of Pb ions within the octahedra, Pb ions have smaller amplitudes of atomic vibration and thus a smaller average value of δ than I ions (see **Figure 1b**). With increasing temperature, some I ions reach their δ_{cr} and become Lindemann particles. This corresponds to the breaking of the octahedral network by splitting of the PbI_6 octahedron. The accumulation of octahedral network defects (Lindemann particles of I^- ions) finally gives rise to a global lattice instability of the whole structure. In the defective $MAPbI_3$ crystals, ions in the vicinity of vacancies are less constrained by the electrostatic interactions, and have larger amplitudes of atomic vibrations compared to those in the pristine crystal (see **Figure S4** in **Supporting Information**). Thus the accumulation of the local lattice instabilities in defective crystals is faster than in the pristine crystal, resulting in the global lattice instability of defective crystals at lower temperature.

3.5 Thermal instability in polycrystalline $MAPbI_3$ crystals

Finally, we investigate the impact of two-dimensional defects such as twin boundaries and grain boundaries of the instability of $MAPbI_3$ crystals by considering bicrystal and polycrystal models of varying grain sizes. **Figure 8** presents the key results for a bicrystal as well as a polycrystalline structure for brevity, whereas the determination of critical temperatures T_c at which the crystal instability occurs in other polycrystalline cases are illustrated in detail in **Figures S5** in E**SI**. It can be seen that in the simpler case of bi-crystalline $MAPbI_3$, for twin boundaries of both Σ5(2 1 0) and Σ10(3 1 0)) orientations, T_c is approximately 640 K, which is much lower than that in the case of pristine crystal structure (~1050 K) as well as the crystal with point defects at large concentrations (840 K – 960 K) As for the polycrystalline $MAPbI_3$, randomly oriented GBs further decrease T_c to within the range of 550 K to 570 K. Interestingly, these predicted values for T_c are quite close to the instability temperature (from 520 K to 690 K) measured by thermogravimetric analysis (520 K – 690 K).[11, 14, 16-21] An analysis of the microstructural evolution of grain boundaries indicates that with increasing temperature, the concentration of point defects as well as the size of the amorphous regions in the vicinity of grain boundaries increasing, triggering the thermal instability of $MAPbI_3$ polycrystals at a much lower temperature. The good agreement between our computational and previous experimental results confirms the validity of our atomistic modelling of thermal instability of $MAPbI_3$.

3.6 Summary of thermal instability in $MAPbI_3$

Figure 9 summarizes the critical temperatures for the onset of the instability in $MAPbI_3$ crystals for all cases considered in our work and compares against the typical range of experimental values

reported in literature. It is evident that, in general, two-dimensional defects such as free surfaces and twin/grain boundaries are responsible for the early onset of the instability of $MAPbI_3$ crystals. Remarkably, T_c values predicted for single crystal thin films or polycrystals are within the range of experimental values as shown in **Figure 9**. We emphasize that the models presented here consider only one type of defect at a time. In contrast, the polycrystalline thin films used in experiments are characterized by a multitude of such defects, all occurring simultaneously. As a result, the interplay between various kinds of defects (in particular, a triple junction of grain boundaries with free surfaces) is likely to lead to a much earlier onset of the crystal instability, with much lower T_c than reported here. Furthermore, here we have ignored the effect of defect migration on the stability of $MAPbI_3$ crystal, as the time scale for the defect migration is much longer than that of the simulations. Since elevated temperatures accelerate the migration of defects and subsequently, the formation of aggregated defect clusters (i.e. nanovoids),[31, 35] it can be anticipated that considering kinetics of defects can also lead to an earlier onset of crystal instability with lower T_c values.

We have demonstrated here that the thermal instabilities in $MAPbI_3$ crystals are closely associated with their microstructural evolution such as tilting and splitting of PbI_6 octahedra. This suggests that a design of new hybrid perovskites with enhanced thermal stability should in principle be possible by suppressing the tilting of their octahedra. For example, one can substitute few or all of the ionic components (MA^+, Pb^{2+}, I^-) of prototype $MAPbI_3$ by other ionic species, such as formamidinium ($HN{=}CHNH^{3+}$, or FA^+), Cs^+, Br^-, or Cl^-. Few recent studies have experimentally found that substituting MA^+ ions by a low doping concentration of larger ions (i.e. FA^+) can enhance their thermal stability, which can be attributed to a global locking of PbI_6 octahedra.[24, 83,

[84] Our simulations also show that the thermal instability of hybrid perovskites initiates from their intrinsic structural defects, and greatly reduce the applicability of such materials at elevated temperatures. This highlights the importance of further exploring the material design strategies, such as surface passivation or interface strengthening, to minimize the detrimental influence of intrinsic defects on the thermal stability of hybrid perovskites. Furthermore, strategies such as lowering perovskite dimensions or increasing the valence charge of ions, can suppress defect/ion migration and clustering, thereby further improving the material stability.[31, 85]

4. Conclusions

In conclusion, we investigated the molecular mechanisms of structural instability in $MAPbI_3$ bulk crystals and polycrystalline thin films. Large-scale MD simulations show that pristine $MAPbI_3$ crystal maintains its crystalline integrity until a critical temperature (T_c) as large as ~1050 K, at which it undergoes a crystalline to amorphous phase transition. We establish the underlying relationships between the thermal instability and microstructural evolution in $MAPbI_3$ crystals. With increasing temperature, the thermal instability in $MAPbI_3$ crystals is preceded by a continuous softening of their octahedral network, associated with the tilting and splitting of PbI_6 octahedra. Point vacancies, especially the partial Schottky MAI^0 vacancies, accelerate the initiation of local lattice instability, leading to the crystal decomposition of $MAPbI_3$ crystals at much lower temperatures (i.e. a decrease in T_c of ~250 K for MAI^0 vacancies at a concentration of 3%). The predictions of phonon modes confirm the tilting and splitting of PbI_6 octahedra in defective $MAPbI_3$ crystals. We also explored the thermal instability in bi-crystalline and polycrystalline $MAPbI_3$ crystals and demonstrated that grain boundaries can reduce the crystal instability temperature to about 550 K, close to the experimental measurement by

thermogravimetric analysis. Our results suggest that both Born (mechanical) and Lindemann (thermodynamic) criteria coincide in governing the thermal instability by the initiation and accumulation of local lattice instabilities. Consistent with Lindemann criterion, thermal instability in thin films originates from their free surfaces at much lower temperatures due the increased free energies of $MAPbI_3$ thin films. Specifically, thermal instability initiates from the charge neutral $(100)/[MAI]^0$ surface at lower temperature than that from the $(100)/[PbI_2]^0$ surface. The analysis of the thermal instability in the prototypical hybrid perovskite $MAPbI_3$ presented here can provide guidance on the optimal selection and rational design of hybrid perovskite functional components with enhanced thermal stability for efficient and stable energy harvesting and conversion applications. Furthermore, the analysis presented here can also be extended to study the low-dimensional perovskites, which have recently been demonstrated with an improved stability compared to their three-dimensional counterparts.[23]

Acknowledgements

M.W., N.B. and N.V.M. acknowledge support from the Monash University Cluster, the Australian National Computing Infrastructure (NCI), and the Pawsey Supercomputing Centre for high performance computing, and the financial support from Australian Research Council's Discovery Project scheme (DP160103661). S.L. acknowledges startup funding from the Energy and Materials Initiative from the Florida State University and funding from the National Science Foundation (NSF-CBET-1708968).

References

1. M. M. Lee, J. Teuscher, T. Miyasaka, T. N. Murakami and H. J. Snaith, *Science*, 2012, **338**, 643-647.

2. J. Burschka, N. Pellet, S.-J. Moon, R. Humphry-Baker, P. Gao, M. K. Nazeeruddin and M. Gratzel, *Nature*, 2013, **499**, 316-319.
3. M. Saliba, T. Matsui, K. Domanski, J.-Y. Seo, A. Ummadisingu, S. M. Zakeeruddin, J.-P. Correa-Baena, W. R. Tress, A. Abate, A. Hagfeldt and M. Grätzel, *Science*, 2016, **354**, 206-209.
4. J.-P. Correa-Baena, A. Abate, M. Saliba, W. Tress, T. Jesper Jacobsson, M. Grätzel and A. Hagfeldt, *Energy Environ. Sci.*, 2017, **10**, 710-727.
5. K. A. Bush, A. F. Palmstrom, Z. J. Yu, M. Boccard, R. Cheacharoen, J. P. Mailoa, D. P. McMeekin, R. L. Z. Hoye, C. D. Bailie, T. Leijtens, I. M. Peters, M. C. Minichetti, N. Rolston, R. Prasanna, S. Sofia, D. Harwood, W. Ma, F. Moghadam, H. J. Snaith, T. Buonassisi, Z. C. Holman, S. F. Bent and M. D. McGehee, *Nat. Energy*, 2017, **2**, 17009.
6. T. Duong, Y. Wu, H. Shen, J. Peng, X. Fu, D. Jacobs, E.-C. Wang, T. C. Kho, K. C. Fong, M. Stocks, E. Franklin, A. Blakers, N. Zin, K. McIntosh, W. Li, Y.-B. Cheng, T. P. White, K. Weber and K. Catchpole, *Adv. Energy Mater.*, 2017, **7**, 1700228.
7. J. H. Noh, S. H. Im, J. H. Heo, T. N. Mandal and S. I. Seok, *Nano Lett.*, 2013, **13**, 1764-1769.
8. N.-K. Kim, Y. H. Min, S. Noh, E. Cho, G. Jeong, M. Joo, S.-W. Ahn, J. S. Lee, S. Kim, K. Ihm, H. Ahn, Y. Kang, H.-S. Lee and D. Kim, *Sci. Rep.*, 2017, **7**, 4645.
9. L. Meng, J. You and Y. Yang, *Nat. Commun.*, 2018, **9**, 5265.
10. X. Yu, Y. Qin and Q. Peng, *J. Phys. Chem. A*, 2017, **121**, 1169-1174.
11. T. Baikie, Y. Fang, J. M. Kadro, M. Schreyer, F. Wei, S. G. Mhaisalkar, M. Graetzel and T. J. White, *J. Mater. Chem. A*, 2013, **1**, 5628-5641.
12. C. C. Stoumpos, C. D. Malliakas and M. G. Kanatzidis, *Inorg. Chem.*, 2013, **52**, 9019-9038.
13. A. Dualeh, N. Tétreault, T. Moehl, P. Gao, M. K. Nazeeruddin and M. Grätzel, *Adv. Funct. Mater.*, 2014, **24**, 3250-3258.
14. E. J. Juarez-Perez, Z. Hawash, S. R. Raga, L. K. Ono and Y. Qi, *Energy Environ. Sci.*, 2016, **9**, 3406-3410.
15. A. Ciccioli and A. Latini, *J. Phys. Chem. Lett.*, 2018, **9**, 3756-3765.
16. L. Dimesso, M. Dimamay, M. Hamburger and W. Jaegermann, *Chem. Mater.*, 2014, **26**, 6762-6770.
17. A. Dualeh, P. Gao, S. I. Seok, M. K. Nazeeruddin and M. Grätzel, *Chem. Mater.*, 2014, **26**, 6160-6164.
18. D. P. Nenon, J. A. Christians, L. M. Wheeler, J. L. Blackburn, E. M. Sanehira, B. Dou, M. L. Olsen, K. Zhu, J. J. Berry and J. M. Luther, *Energy Environ. Sci.*, 2016, **9**, 2072-2082.
19. A. E. Williams, P. J. Holliman, M. J. Carnie, M. L. Davies, D. A. Worsley and T. M. Watson, *J. Mater. Chem. A*, 2014, **2**, 19338-19346.
20. W. Zhang, M. Saliba, D. T. Moore, S. K. Pathak, M. T. Hörantner, T. Stergiopoulos, S. D. Stranks, G. E. Eperon, J. A. Alexander-Webber, A. Abate, A. Sadhanala, S. Yao, Y. Chen, R. H. Friend, L. A. Estroff, U. Wiesner and H. J. Snaith, *Nat. Commun.*, 2015, **6**, 6142.
21. J. H. Heo, S. H. Im, J. H. Noh, T. N. Mandal, C.-S. Lim, J. A. Chang, Y. H. Lee, H.-j. Kim, A. Sarkar, M. K. Nazeeruddin, M. Grätzel and S. I. Seok, *Nat. Photonics*, 2013, **7**, 486.
22. B. Conings, J. Drijkoningen, N. Gauquelin, A. Babayigit, J. D'Haen, L. D'Olieslaeger, A. Ethirajan, J. Verbeeck, J. Manca, E. Mosconi, F. D. Angelis and H.-G. Boyen, *Adv. Energy Mater.*, 2015, **5**, 1500477.
23. T. Zhang, M. I. Dar, G. Li, F. Xu, N. Guo, M. Grätzel and Y. Zhao, *Sci. Adv.*, 2017, **3**, e1700841.
24. D. P. McMeekin, G. Sadoughi, W. Rehman, G. E. Eperon, M. Saliba, M. T. Hörantner, A. Haghighirad, N. Sakai, L. Korte, B. Rech, M. B. Johnston, L. M. Herz and H. J. Snaith, *Science*, 2016, **351**, 151-155.
25. Z. Wang, Q. Lin, F. P. Chmiel, N. Sakai, L. M. Herz and H. J. Snaith, *Nat. Energy*, 2017, **2**, 17135.
26. J. Kim, S.-H. Lee, J. H. Lee and K.-H. Hong, *J. Phys. Chem. Lett.*, 2014, **5**, 1312-1317.
27. N. Aristidou, C. Eames, I. Sanchez-Molina, X. Bu, J. Kosco, M. S. Islam and S. A. Haque, *Nat. Commun.*, 2017, **8**, 15218.
28. D. W. de Quilettes, S. M. Vorpahl, S. D. Stranks, H. Nagaoka, G. E. Eperon, M. E. Ziffer, H. J. Snaith and D. S. Ginger, *Science*, 2015, **348**, 683-686.
29. Y. Shao, Y. Fang, T. Li, Q. Wang, Q. Dong, Y. Deng, Y. Yuan, H. Wei, M. Wang, A. Gruverman, J. Shield and J. Huang, *Energy Environ. Sci.*, 2016, **9**, 1752-1759.

30. X. Li, M. Ibrahim Dar, C. Yi, J. Luo, M. Tschumi, S. M. Zakeeruddin, M. K. Nazeeruddin, H. Han and M. Grätzel, *Nat. Chem.*, 2015, **7**, 703.
31. Y. Yuan and J. Huang, *Acc. Chem. Res.*, 2016, **49**, 286-293.
32. Q. Wang, B. Chen, Y. Liu, Y. Deng, Y. Bai, Q. Dong and J. Huang, *Energy Environ. Sci.*, 2017, **10**, 516-522.
33. C. Eames, J. M. Frost, P. R. F. Barnes, B. C. O'Regan, A. Walsh and M. S. Islam, *Nat. Commun.*, 2015, **6**, 7497.
34. H. Yuan, E. Debroye, K. Janssen, H. Naiki, C. Steuwe, G. Lu, M. Moris, E. Orgiu, H. Uji-i, F. De Schryver, P. Samorì, J. Hofkens and M. Roeffaers, *J. Phys. Chem. Lett.*, 2016, **7**, 561-566.
35. P. Delugas, C. Caddeo, A. Filippetti and A. Mattoni, *J. Phys. Chem. Lett.*, 2016, **7**, 2356-2361.
36. H. J. Snaith, A. Abate, J. M. Ball, G. E. Eperon, T. Leijtens, N. K. Noel, S. D. Stranks, J. T.-W. Wang, K. Wojciechowski and W. Zhang, *J. Phys. Chem. Lett.*, 2014, **5**, 1511-1515.
37. S. Meloni, T. Moehl, W. Tress, M. Franckevičius, M. Saliba, Y. H. Lee, P. Gao, M. K. Nazeeruddin, S. M. Zakeeruddin, U. Rothlisberger and M. Graetzel, *Nat. Commun.*, 2016, **7**, 10334.
38. Z. Xiao, Y. Yuan, Y. Shao, Q. Wang, Q. Dong, C. Bi, P. Sharma, A. Gruverman and J. Huang, *Nat. Mater.*, 2014, **14**, 193.
39. A. Walsh, D. O. Scanlon, S. Chen, X. G. Gong and S.-H. Wei, *Angew. Chem. Int.*, 2015, **54**, 1791-1794.
40. W.-J. Yin, T. Shi and Y. Yan, *Appl. Phys. Lett.*, 2014, **104**, 063903.
41. E. Mosconi, J. M. Azpiroz and F. De Angelis, *Chem. Mater.*, 2015, **27**, 4885-4892.
42. L. Zhang, M.-G. Ju and W. Liang, *Phys. Chem. Chem. Phys.*, 2016, **18**, 23174-23183.
43. A. Mattoni, A. Filippetti, M. I. Saba and P. Delugas, *J. Phys. Chem. C*, 2015, **119**, 17421-17428.
44. M. Wang and S. Lin, *Adv. Funct. Mater.*, 2016, **26**, 5297-5306.
45. J. Yu, M. Wang and S. Lin, *ACS Nano*, 2016, **10**, 11044-11057.
46. C. Caddeo, M. I. Saba, S. Meloni, A. Filippetti and A. Mattoni, *ACS Nano*, 2017, **11**, 9183-9190.
47. H. Zhou, J. Wang, M. Wang and S. Lin, *ACS Appl. Mater. Interfaces*, 2020, **12**, 23584-23594.
48. S. Plimpton, *J. Comput. Phys.*, 1995, **117**, 1-19.
49. J. Wang, L. Zhao, M. Wang and S. Lin, *Cryst. Growth Des.*, 2017, **17**, 6201-6211.
50. R. W. Hockney and J. W. Eastwood, *Computer Simulation Using Particles*, crc Press, 1988.
51. M. P. Allen and D. J. Tildesley, *Computer Simulation of Liquids*, Oxford university press, 1989.
52. C.-J. Tong, W. Geng, Z.-K. Tang, C.-Y. Yam, X.-L. Fan, J. Liu, W.-M. Lau and L.-M. Liu, *J. Phys. Chem. Lett.*, 2015, **6**, 3289-3295.
53. J. Haruyama, K. Sodeyama, L. Han and Y. Tateyama, *Acc. Chem. Res.*, 2016, **49**, 554-561.
54. S. Nosé, *J. Chem. Phys.*, 1984, **81**, 511-519.
55. W. G. Hoover, *Phys. Rev. A*, 1985, **31**, 1695-1697.
56. Z. H. Jin, P. Gumbsch, K. Lu and E. Ma, *Phys. Rev. Lett.*, 2001, **87**, 055703.
57. M. Born, *J. Chem. Phys.*, 1939, **7**, 591-603.
58. D. Wolf, P. R. Okamoto, S. Yip, J. F. Lutsko and M. Kluge, *J. Mater. Res.*, 2011, **5**, 286-301.
59. J. R. Ray, *Comput. Phys. Rep.*, 1988, **8**, 109-151.
60. G. Gao, K. V. Workum, J. D. Schall and J. A. Harrison, *J. Phys. Condens. Matter*, 2006, **18**, S1737-S1750.
61. L. T. Kong, G. Bartels, C. Campañá, C. Denniston and M. H. Müser, *Comput. Phys. Commun.*, 2009, **180**, 1004-1010.
62. J. L. Tallon, *Philos. Mag. Lett.*, 1979, **39**, 151-161.
63. A. Samanta, M. E. Tuckerman, T.-Q. Yu and W. E, *Science*, 2014, **346**, 729-732.
64. M. Forsblom and G. Grimvall, *Nat. Mater.*, 2005, **4**, 388.
65. Z. Wang, F. Wang, Y. Peng, Z. Zheng and Y. Han, *Science*, 2012, **338**, 87-90.
66. L. D. Whalley, J. M. Frost, Y.-K. Jung and A. Walsh, *J. Chem. Phys.*, 2017, **146**, 220901.
67. K. Wakamura, *Phys. Rev. B*, 1997, **56**, 11593-11599.
68. Y. Yang, F. Gao, S. Gao and S.-H. Wei, *J. Mater. Chem. A*, 2018, **6**, 14949-14955.
69. W. Luo and W. Hu, *Physica B Condens. Matter*, 2013, **425**, 90-94.

70. H. A. Alarifi, M. Atiş, C. Özdoğan, A. Hu, M. Yavuz and Y. Zhou, *J. Phys. Chem. C*, 2013, **117**, 12289-12298.
71. Q. S. Mei and K. Lu, *Prog. Mater. Sci.*, 2007, **52**, 1175-1262.
72. X.-M. Bai and M. Li, *J. Chem. Phys.*, 2005, **123**, 151102.
73. X.-M. Bai and M. Li, *Nano Lett.*, 2006, **6**, 2284-2289.
74. L. She, M. Liu and D. Zhong, *ACS Nano*, 2016, **10**, 1126-1131.
75. J. Jagielski, S. Kumar, M. Wang, D. Scullion, R. Lawrence, Y.-T. Li, S. Yakunin, T. Tian, M. V. Kovalenko, Y.-C. Chiu, E. J. G. Santos, S. Lin and C.-J. Shih, *Sci. Adv.*, 2017, **3**, eaaq0208.
76. Z. Fan, H. Xiao, Y. Wang, Z. Zhao, Z. Lin, H.-C. Cheng, S.-J. Lee, G. Wang, Z. Feng, W. A. Goddard, Y. Huang and X. Duan, *Joule*, 2017, **1**, 548-562.
77. F. Lindemann, *Phys. Z.*, 1910, **11**, 609.
78. R. W. Cahn, *Nature*, 1986, **323**, 668-669.
79. R. N. Barnett and U. Landman, *Phys. Rev. B*, 1991, **44**, 3226-3239.
80. F. H. Stillinger and T. A. Weber, *Phys. Rev. B*, 1980, **22**, 3790-3794.
81. R. Agrawal and D. A. Kofke, *Mol. Phys.*, 1995, **85**, 23-42.
82. R. W. Cahn, *Nature*, 2001, **413**, 582-583.
83. G. E. Eperon, S. D. Stranks, C. Menelaou, M. B. Johnston, L. M. Herz and H. J. Snaith, *Energy Environ. Sci.*, 2014, **7**, 982-988.
84. F. C. Hanusch, E. Wiesenmayer, E. Mankel, A. Binek, P. Angloher, C. Fraunhofer, N. Giesbrecht, J. M. Feckl, W. Jaegermann, D. Johrendt, T. Bein and P. Docampo, *J. Phys. Chem. Lett.*, 2014, **5**, 2791-2795.
85. Y. Lin, Y. Bai, Y. Fang, Q. Wang, Y. Deng and J. Huang, *ACS Energy Lett.*, 2017, **2**, 1571-1572.

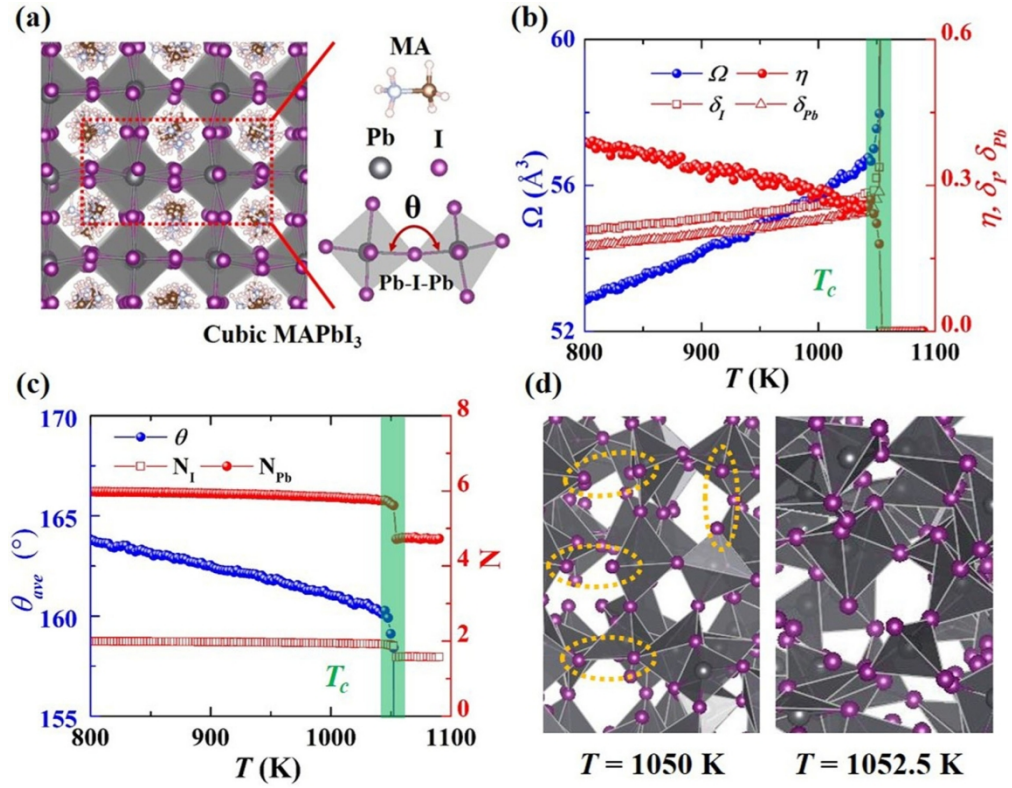

Figure 1. Thermal instability and evolution of crystal structure in pristine $MAPbI_3$. (a) Atomistic configuration of $MAPbI_3$ crystal at room temperature. θ denotes the Pb-I-Pb octahedral tilting angle. (b) The mean atomic volume (Ω), translational order parameter (η), and Lindemann ratios for Pb (δ_{Pb}) and I (δ_I) ions as a function of temperature. (c) Averaged octahedral tilting angle (θ_{ave}), and coordination numbers for Pb (N_{Pb}) and I (N_I) ions as a function of temperature. (d) Atomic structure of $MAPbI_3$ crystal close to the critical transition temperature T_c, at T = 1050 (left) and 1052.5 K (right). The dashed orange circles highlight the dangling Pb-I bonds of partial PbI_6 octahedra in the $MAPbI_3$ crystal.

160x125mm (300 x 300 DPI)

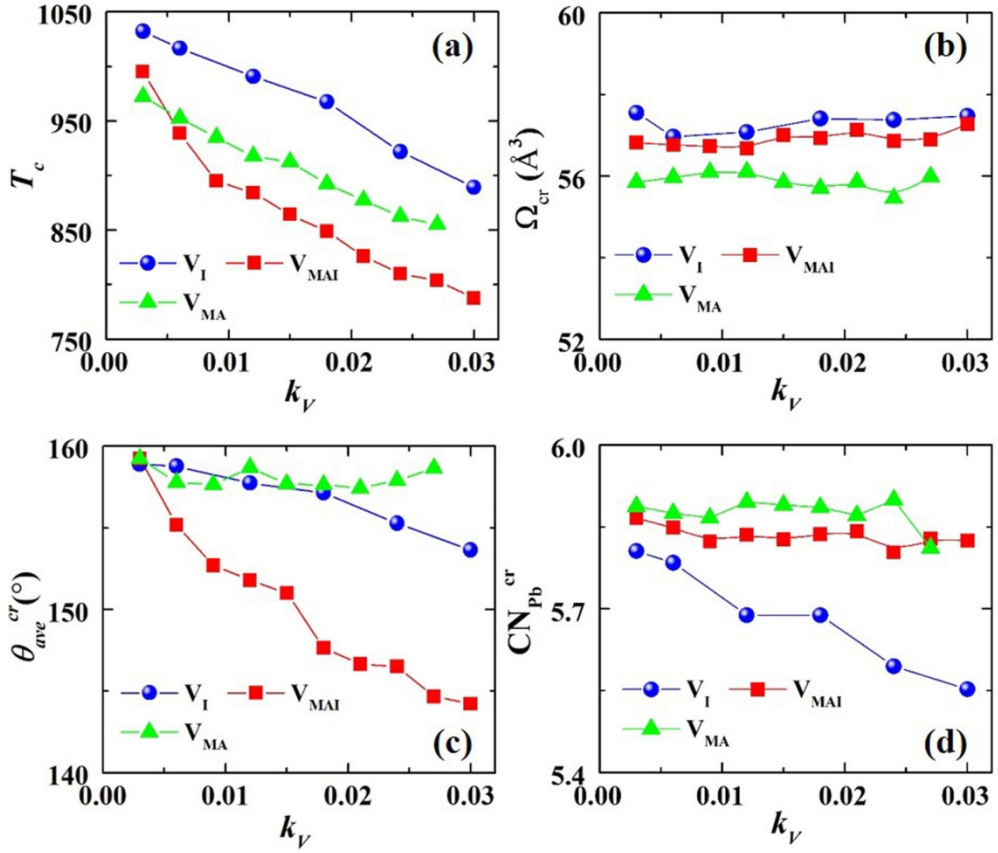

Figure 2. Thermal instability and evolution of crystal structure in $MAPbI_3$ with point defects. (a-b) show the predicted critical thermal instability temperature (T_C) (a), and the critical values of mean atomic volume (Ω_{cr}) (b) with respect to the vacancy concentration k_V. (c-d) show the microstructural parameters, such as the averaged critical tilting angle (θ_{ave}^{cr}) (c) and the critical value of the coordination number for Pb ions (N_{Pb}^{cr}) at T_c with respect to k_V (d). Several types of point defects, including I^- (V_I), MA^+ (V_{MA}), and MAI^0 (V_{MAI}) vacancies are considered here.

159x137mm (300 x 300 DPI)

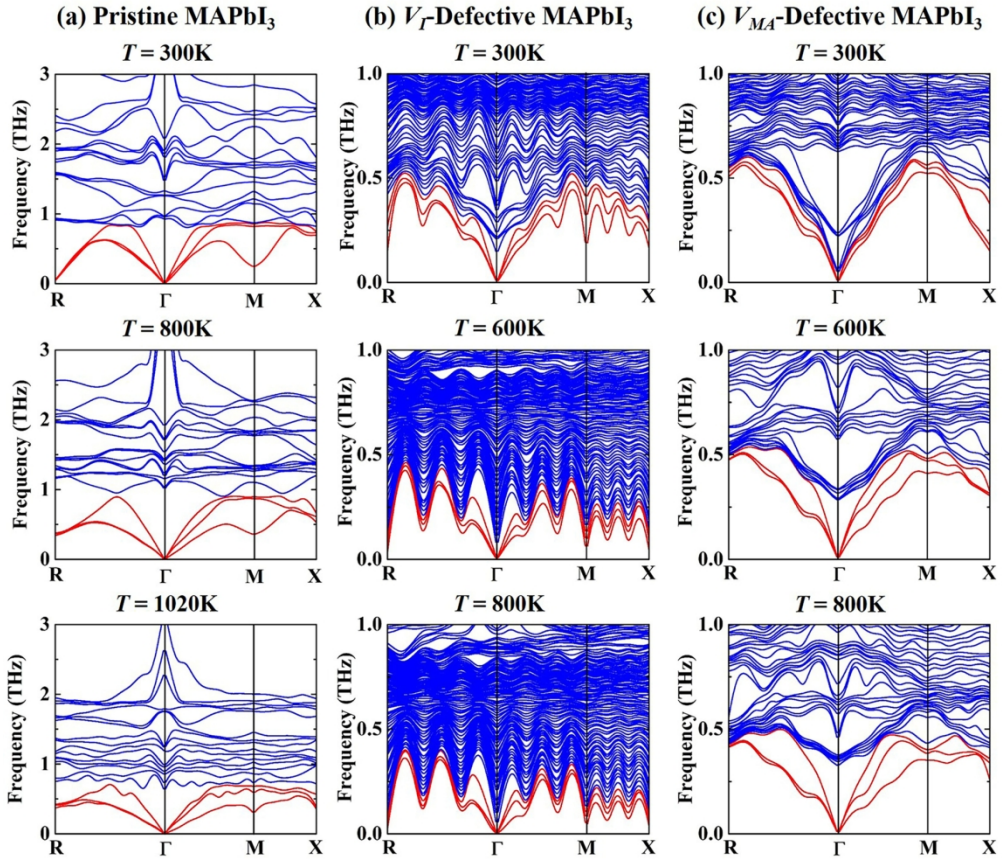

Figure 3. Phonon dispersion curves of pristine and defective $MAPbI_3$ with point defects. (a) Pristine and (b-c) defective hybrid perovskite $MAPbI_3$ with I^- (b) and MA^+ (c) vacancy defects at a concentration of k_V = 0.025 at different temperatures. All phonon branches are determined within the first Brillouin zone. *R*, *Γ*, *M* and *X* represent the (0.5 0.5 0.5), (0 0 0), (0.5 0.5 0), and (0 0.5 0) points in the reciprocal space. Acoustic and optical phonon modes are indicated by red and blue colors, respectively.

159x138mm (300 x 300 DPI)

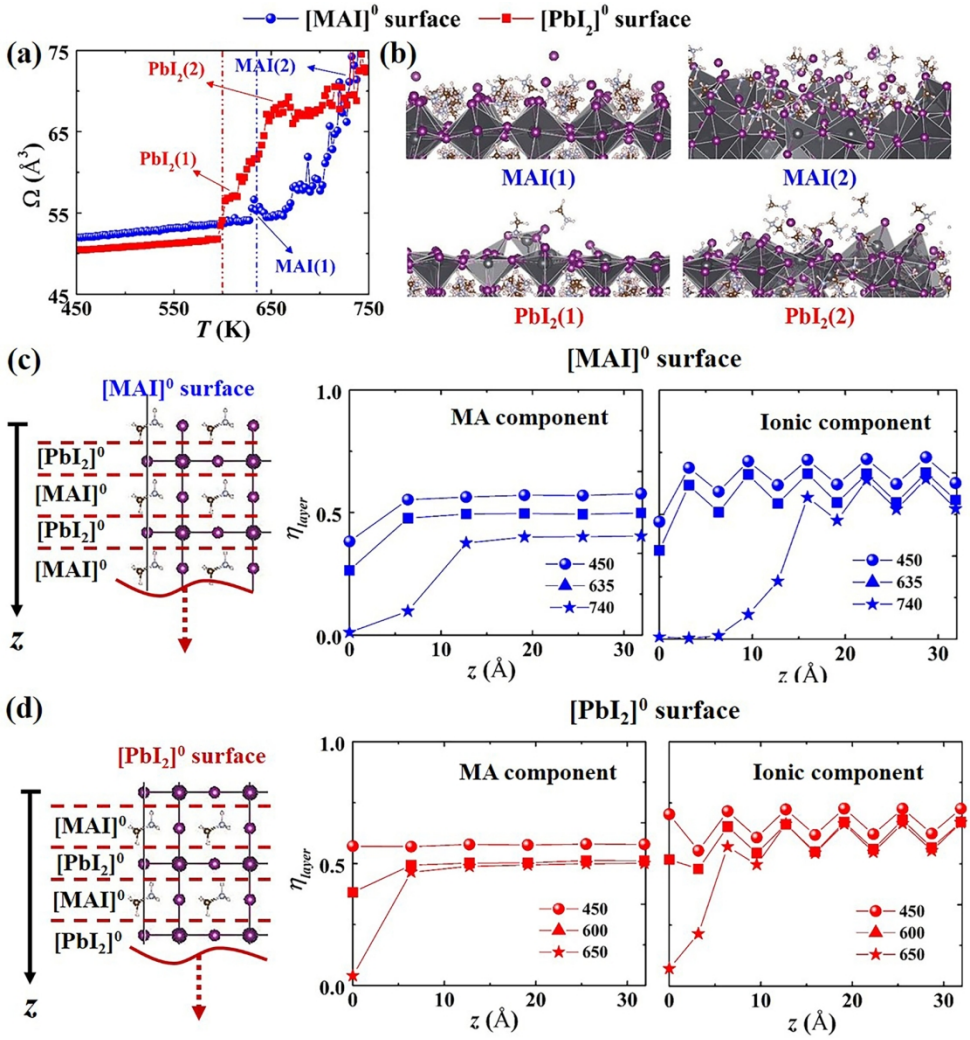

Figure 4. Thermal decomposition and microstructural evolution of $[MAI]^0$- and $[PbI_2]^0$-terminated $MAPbI_3$ thin films. (a) The mean atomic volume (Ω) as a function of temperature (T). (b) Snapshots of the atomic configurations of partial and complete decomposition of $[MAI]^0$ and $[PbI_2]^0$ free surfaces as highlighted in (a). (c) In-plane layer order parameter η_{layer} for $[MA]^{n+}$ and ionic ($[PbI_2]^0$ and $[I]^{n-}$) components in the $[MAI]^0$-terminated thin film, as a function of the distance from the free surface (z). (d) In-plane layer order parameter η_{layer} for $[MA]^{n+}$ and ionic ($[PbI_2]^0$ and $[I]^{n-}$) components in $[PbI_2]^0$-terminated thin film, as a function of the distance from the free surface (z).

160x166mm (300 x 300 DPI)

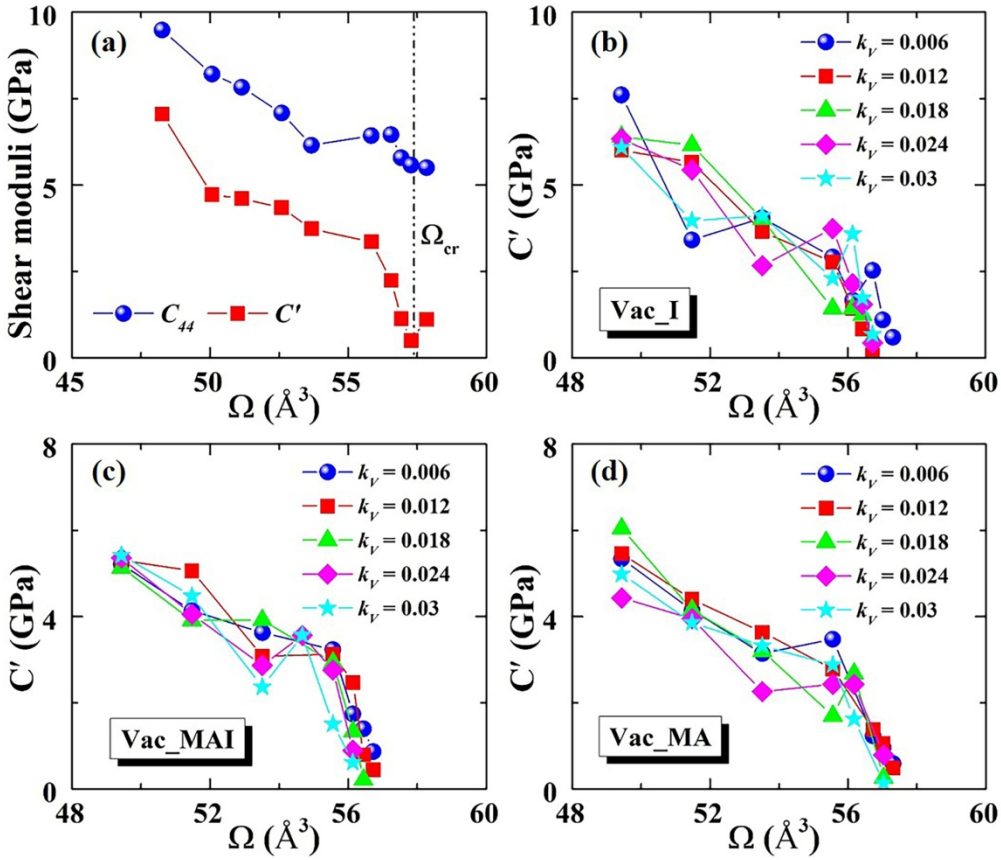

Figure 5. Shear moduli of pristine and defective $MAPbI_3$ crystals with respect to mean atomic volume. (a) The shear moduli C_{44} and C' of pristine bulk $MAPbI_3$ with respect to the mean atomic volume (Ω). (b-d) The shear modulus C' of defective bulk $MAPbI_3$ with (b) I^- (V_I), (c) MA^+ (V_{MA}), and (d) MAI^0 (V_{MAI}) vacancies with respect to the mean atomic volume (Ω) for different vacancy concentrations k_V.

160x138mm (300 x 300 DPI)

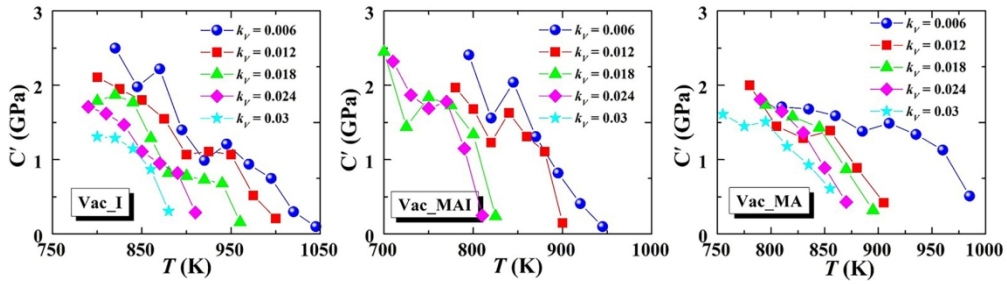

Figure 6. Shear moduli *C′* of defective $MAPbI_3$ crystals with respect to temperature. Various types of vacancies, including I^- (V_I), MA^+ (V_{MA}), and MAI^0 (V_{MAI}), as well as vacancy concentrations k_V in the range of 0.006 to 0.03 are considered, respectively.

160x44mm (300 x 300 DPI)

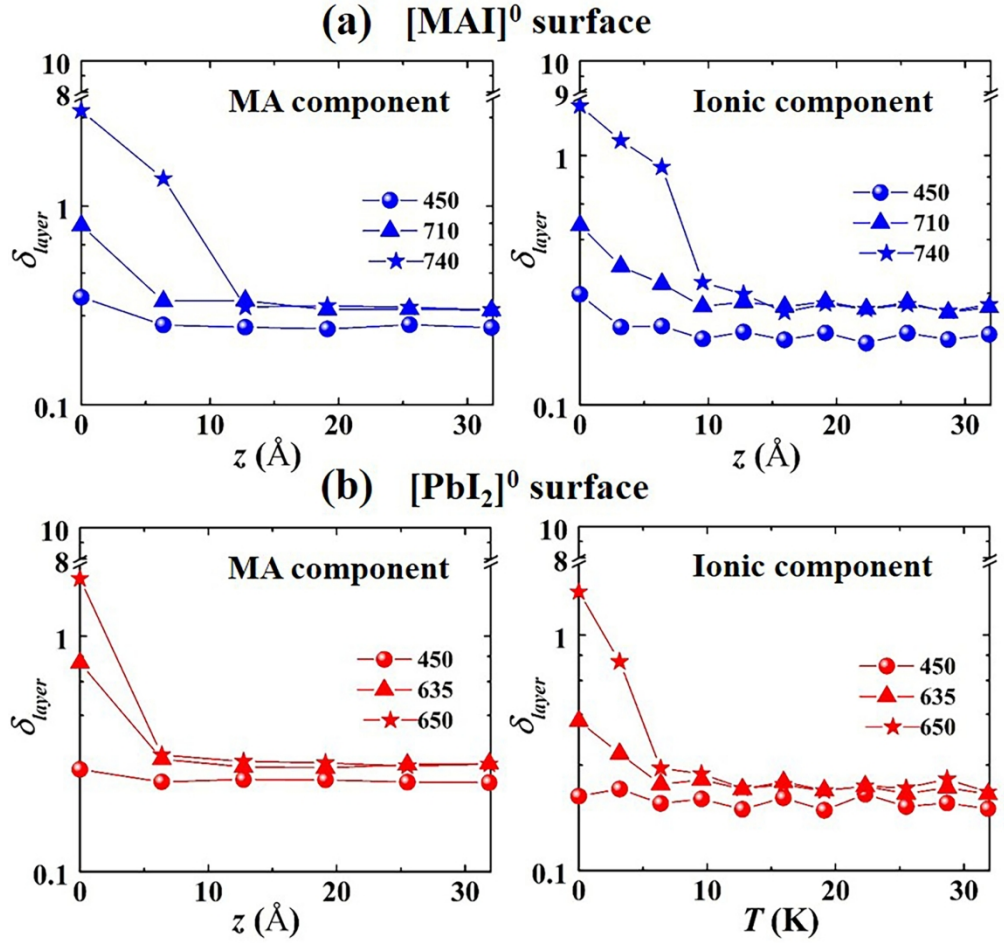

Figure 7. Lindemann ratio of $[MAI]^0$- and $[PbI_2]^0$-terminated $MAPbI_3$ thin films. Layer average Lindemann δ_{layer} of $[MA]^{n+}$ and ionic ($[PbI_2]^0$ and $[I]^{n-}$) components in (a) $[MAI]^0$-terminated and (b) $[PbI_2]^0$-terminated thin films, as a function of distance from the free surface (z), as a function of distance from the free surface (z). z denotes the distance from the free surface as shown in Figure 4.

159x154mm (300 x 300 DPI)

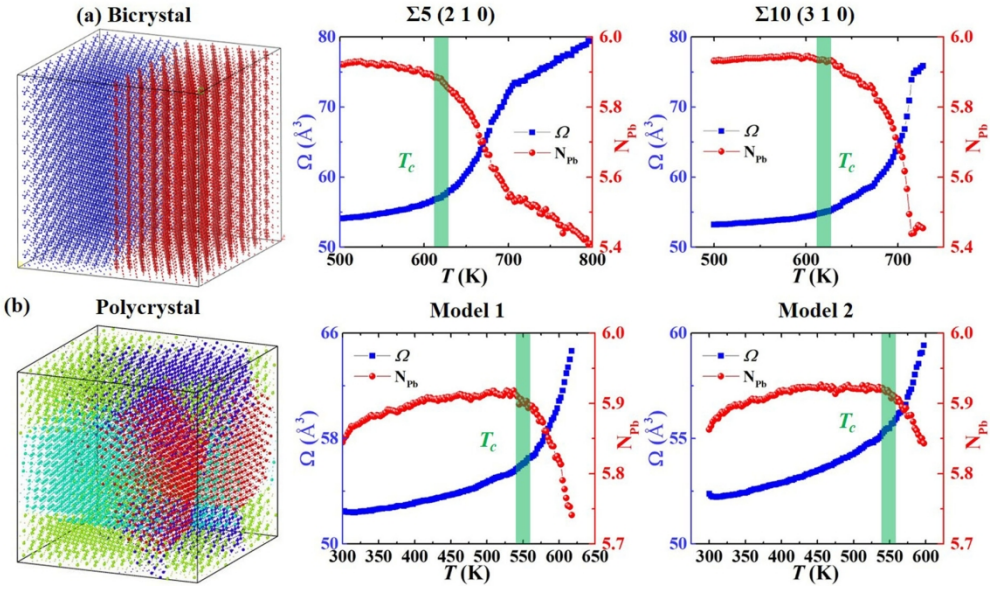

Figure 8. Thermal instability in bicrystals and polycrystals. Atomistic configurations, as well as the mean atomic volume (Ω) and averaged coordination number of Pb ions (N_{Pb}) with respect to temperature for (a) $MAPbI_3$ bicrystal with the symmetric twin boundaries of orientations Σ5(2 1 0), and Σ10(3 1 0), and (b) two polycrystal models with the average grain size of 25 nm^3. Different grains are represented by different colors for visual clarity.

160x94mm (300 x 300 DPI)

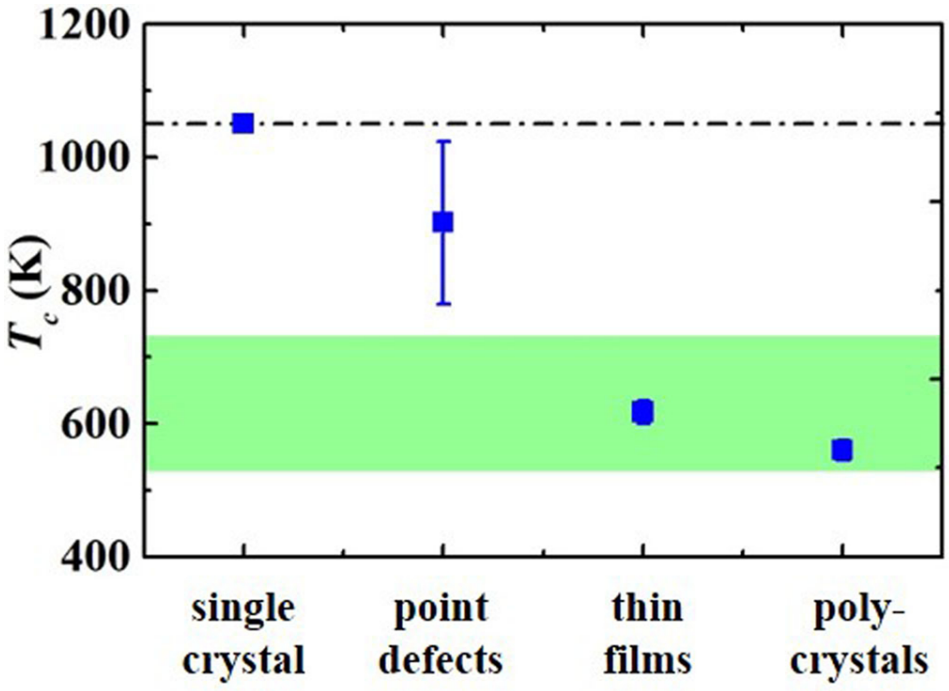

Figure 9. Critical temperature T_C for thermal instability in pristine and defective $MAPbI_3$ crystals. $MAPbI_3$ models include pristine single crystal, single crystals with point defects, thin films, and poly-crystals. The dashed line represents the upper limit of T_C, namely T_C of single crystal $MAPbI_3$. The green area represents the wide range of T_C reported in thermogravimetric experiments.[11, 14, 16-21]

90x63mm (300 x 300 DPI)

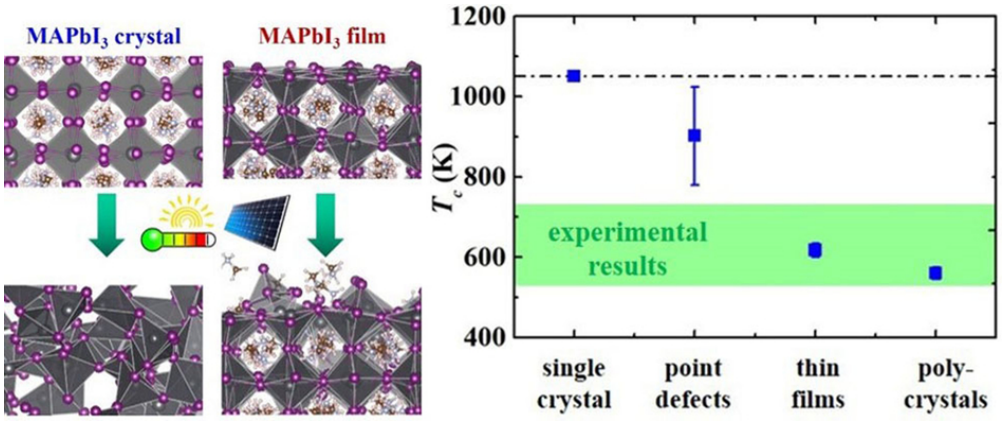

This work explores the molecular-level mechanisms of thermal instability in pristine and defective crystals of the prototypical hybrid perovskite $MAPbI_3$.

79x33mm (300 x 300 DPI)